Journal Name

ARTICLE

Molecular Orientation Unified Nonfullerene Acceptor Enabling 14% Efficiency As-Cast Organic Solar Cells†

Received 00th January 20xx,
Accepted 00th January 20xx

DOI: 10.1039/x0xx00000x

www.rsc.org/

Renyong Geng,[a,‡] Xin Song,[b,‡] Haohao Feng,[a] Jiangsheng Yu,[c] Zhuohan Zhang,[a] Derya Baran[b,*] and Weihua Tang[a,*]

Molecular orientation and π-π stacking of nonfullerene acceptor determine its domain size and purity in the bulk-heterojunction blends with polymer donor. And the interpenetrating networks of donor and acceptor phase play a vital roles in promoting charge transfer for high-efficiency organic solar cells (OSCs) with low energy loss. Two novel nonfullerene acceptors (NFAs) featuring indacenobis(dithieno[3,2-b:2′,3′-d]pyrrol) core with *meta*- or *para*-alkoxyphenyl sidechains on the bridging sp^3 carbon atoms are designed and denoted as ***m*-INPOIC** or ***p*-INPOIC**, respectively. The impact of alkoxyl group positioning on molecular orientation and photovoltaic performance of NFAs is revealed through a comparison study with the counterparts bearing *para*-alkylphenyl (**INPIC-4F**) sidechains. With inward constriction toward the conjugated backbone, ***m*-INPOIC** presents predominant face-on orientation to promote charge transport. The OSCs by blending ***m*-INPOIC** and PBDB-T as active layers exhibit a power conversion efficiency (PCE) of 12.1% without any processing additive or post-device treatment. By introducing $PC_{71}BM$ as the solid processing-aid, the binary OSCs was further optimized to deliver an impressive PCE of 14.0%, which is among the highest PCEs for as-cast single-junction OSCs reported in literature to date. More attractively, PBDB-T:***m*-INPOIC**:$PC_{71}BM$ based OSCs exhibit over 11% PCEs even with active layer thicker than 300 nm. And the devices can retain over 95% PCE after a storage for 20 days. The outstanding tolerance to film thickness and outstanding stability of the as-cast devices make ***m*-INPOIC** a promising candidate NFA for large-scale solution-processable OSCs.

1. Introduction

Organic solar cells (OSCs) have attracted considerable attention because of their unprecedented progress in power conversion efficiency (PCE),[1-5] which now reaches 15.7% in single-junction cells and over 17% in tandem configuration.[6-10] One of the biggest concerns for commercialization of OSCs is the solution-processed active layer, which comprise a donor:acceptor (D:A) bulk heterojunction (BHJ) blend. Elegant device optimization has been developed such as solvent additive processing, vapour annealing[11-13] and thermal annealing treatment[14-16] within thin active layers. Solvent additives have been proved to be more prone to influence the stability and reproducibility of the devices.[17-19] In particular, the compatibility of high-efficiency value and thick blend film is a major challenge as normally the most of the highly efficient OSCs provided their optimal performance with photoactive layer thickness of ≈100 nm.[20] Further increasing the thickness of BHJ film, the complexity of the BHJ morphology would be significantly enhanced, which made it challenging to construct effective charge transport paths in active layer.[21] On the other hand, thin active layer greatly limits the utilization of incident light as well as the real-world application based on the high-throughput roll-to-roll or doctor-blading process, where thick photoactive layer over 300 nm is typically required for the construction of uniform and trap-free film with large-area.

Several groups have reported that the ternary or process-engineering strategy is useful to fabricate thick active films with good PCEs.[20-23] To be noted, most of these devices are based on fullerene derivatives ($PC_{71}BM$ or $PC_{61}BM$) as electron-acceptor on consideration of their excellent electron mobility and isotropic charge transport property. However, fullerene and its derivatives may feature a significant burn-in loss under light soaking, primarily in short-circuited current density (J_{sc}).[24] In addition, the corresponding high-efficiency fullerene-based devices are highly dependent on device optimization,[13] which is difficult to control in large-area printing process and proved to be more prone to influence the stability and reproducibility of the devices. Compared with fullerene acceptors discussed above, non-fullerene acceptors (NFAs) exhibited impressive advantages, for example, broad absorption range, easily adjustable energy levels, tuneable molecular structure and excellent device stability under

[a] *School of Chemical Engineering, Nanjing University of Science and Technology, Nanjing 210094, P.R. China. E-mail: whtang@njust.edu.cn.*
[b] *KAUST Solar Center (KSC), King Abdullah University of Science and Technology (KAUST), Thuwal 23955-6900, Saudi Arabia*
[c] *MIIT Key Laboratory of Advanced Solid Laser, Nanjing University of Science and Technology, Nanjing 210094, P.R. China.*
† *Electronic Supplementary Information (ESI) available: Materials synthesis and characterization, device fabrication, SCLC mobility, GIWAXS and summary of high-efficiency as-cast OSCs in literature. See DOI: 10.1039/x0xx00000x*
‡ *R. G. and X. S. contributed equally to this work.*

Please do not adjust margins

continuous light-irradiation. Recently, Zhan et al.[25] reported a novel NFA with the name of FNIC2, which showing a high electron mobility, face-on orientation and high crystallinity. After blending with PTB7-Th (polymer donor), the champion PCE can be over 13%. Unfortunately, the thicknesses of the corresponding devices are still lower than 200 nm and the stability is not clear.[26] Thus, it is necessary and urgent to design high-efficiency, thickness-insensitive and stable as-cast NFA-OSCs configuration for future commercialization.

Chemical modification is one of the most facile and efficient method to address these challenges.[27-29] Recently, our group have developed an indacenobis(dithieno[3,2-*b*:2′,3′-*d*]pyrrol) (INP) core based NFA (**INPIC-4F**),[30] featuring an extend absorption to 900 nm with an optical bandgap of 1.39 eV. Surprisingly, INPIC-4F is prone to form pronounced spherulites in as-cast devices, resulting in large phase separation and device efficiency below 10%.[31] So in order to engine this molecule for the need of as-cast devices, we herein introduced an individual electron-rich oxygen atoms to increase the intramolecular charge-transfer (ICT) effect of NFA and changed the position of alkoxyl sidechains on phenyl groups in **INPIC-4F** molecule, where the *meta*-substituted and *para*-substituted NFAs are named as ***m*-INPOIC** and ***p*-INPOIC**, respectively. Interestingly, small changes in the substitution position on sidechain exert great influence not only on the optoelectronic properties but also on the molecular packing orientation and crystallinity of the NFA materials. The variation in molecular ordering were found to be related to the distortion of core units with different sidechain modification, which further triggered the dramatic changes in the solubility, molecule planarity and electron mobility of the NFA materials. After blending with PBDB-T, the subtle sidechain engineering induced the significant influence on the carrier recombination, carrier extraction and morphologic feature, and further photovoltaic performance of the corresponding devices. Indeed, benefiting from the preferred "face-on" orientation and intense molecular packing, the as-cast PBDB-T/***m*-INPOIC** OSCs show a PCE of 12.1%, much higher than that of PBDB-T/***p*-INPOIC** (10.6%) and PBDB-T/**INPIC-4F** (9.71%) devices, respectively. When adding $PC_{71}BM$ as solid processing-aid to further manipulate the blend morphology, the as-cast ternary devices obtained a champion PCE of 14.0%. More importantly, the ternary devices exhibit over 11% PCE even with active layer thicker than 300 nm and can retain over 95% PCE after 480 hours storage under N_2 atmosphere.

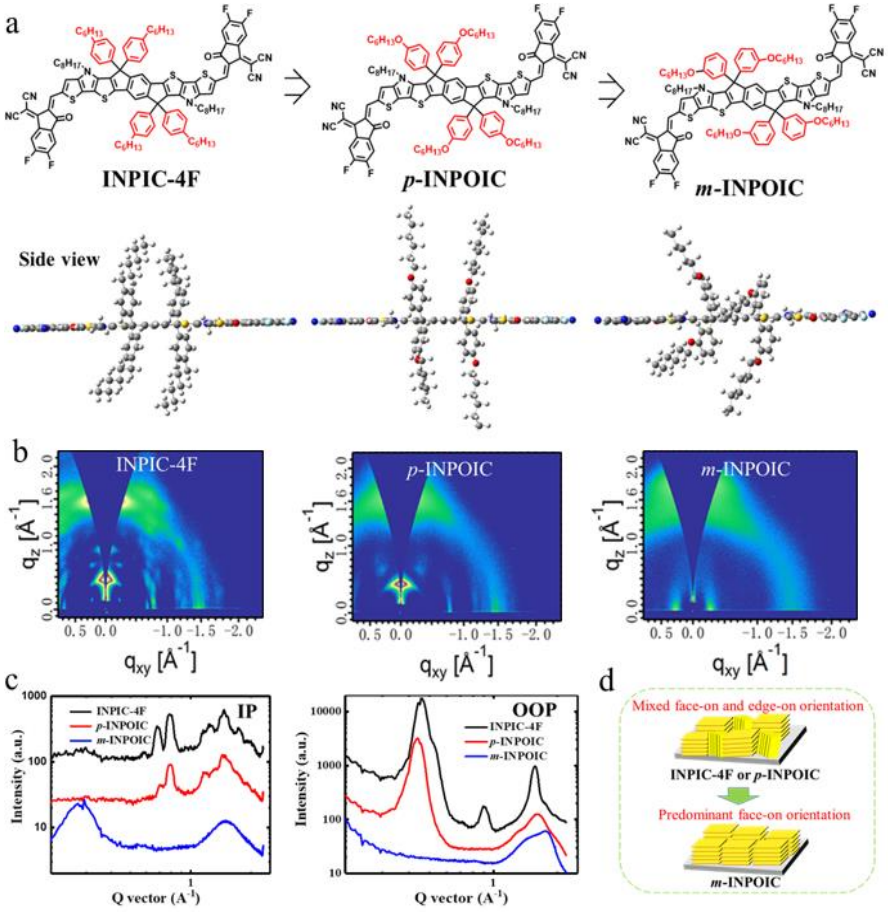

Fig. 1 (a) Chemical structures and simulated geometries of three NFAs. (b) 2D GIWAXS patterns of three NFA neat films. (c) 1D GIWAXS line-cuts of three NFA neat films in the in-plane (IP) and out-of-plane (OOP) direction, where predominant face-on molecular orientation is observed for *m*-INPOIC while mixed face-on and edge-on orientation can be found for both **INPIC-4F** and ***p*-INPOIC**. (d) Schematic diagram for molecular orientation in NFA neat films.

2. Results and discussion

The synthetic route for ***m*-INPOIC** and ***p*-INPOIC** is showed in **Scheme S1** (ESI†). The Knoevenagel condensation between di-

aldehydes of alkoxy-substituted INP cores and fluorinated 3-(dicyanomethylidene)-indan-1-one (2F-IC) is the key step, which afforded ***m*-INPOIC** and ***p*-INPOIC** in 80% and 75% yield, respectively. The detailed procedure and characterizations including ^{1}H NMR, ^{13}C NMR and mass spectra are provided in the Supporting Information (**Fig. S1-S6**, ESI†). The thermal stability of ***m*-INPOIC** and ***p*-INPOIC** was evaluated by thermogravimetric analysis (TGA), with traces shown in **Fig. S7a** (ESI†). A high decomposition temperature (T_d, corresponding to 5% weight loss) ~ 376 ℃ is observed for two alkoxylated NFAs, much higher than that of alkylated INPIC-4F (T_d = 332 ºC).

Density functional theory (DFT) calculation with B3LYP/6-31G(d,p) basic set was employed to investigate the chemical geometries of three acceptors. As observed in **Fig. 1a**, all acceptors show nearly planar molecular configurations from the side view. Thanks to the higher flexibility and planarity of alkoxyl sidechains, ***m*-INPOIC** and ***p*-INPOIC** show more regular alkoxylphenyl orientation as compared to **INPIC-4F**, implying the existence of an O-H attractive interaction. In addition, *meta*-substituted ***m*-INPOIC** exhibits more flexible molecular geometry, mainly due to the *meta*-substitution alkoxylphenyl groups attached INP core. The inward constriction toward molecular backbone may facilitate the intermolecular π-π stacking and unify molecular orientation of ***m*-INPOIC**.[32] The flexible geometry of m-INPOIC may help to enhance the solubility of material. To prove this, we tested the solubility of these three materials in commonly used processing solvent, chlorobenzene. Interestingly, ***m*-INPOIC** show a higher solubility (~ 20 mg/mL) than that of ***p*-INPOIC** (~ 10 mg/mL) and **INPIC-4F** (~ 3 mg/mL). Furthermore, we checked the dissolution condition for as-synthesized NFAs in poor solvents (ethyl acetate).[33] As shown in **Fig. S7b** (ESI†), ***m*-INPOIC** exhibits a better solubility even in the poor solvent in comparison with that of ***p*-INPOIC** and **INPIC-4F**. The enhanced solubility of ***m*-INPOIC** relative to those of ***p*-INPOIC** and **INPIC-4F** would slow down the crystallinity speed during the spinning and drying process. Together with a preferred "face-on" molecular packing of polymer donor and ***m*-INPOIC** materials (will discussed below), thus, a more pronounced "hierarchical morphology" in PBDB-T:***m*-INPOIC** bulk heterojunction blend film is expected, which is beneficial for the efficient exciton dissociation and charge transport.

The ultraviolet-visible (UV-Vis) absorption spectra of the three NFA material were measured in dilute chloroform (see in **Fig. S7c**, ESI†) and in solid state (see in **Fig. 2a**) and the corresponding absorption data are summarized in **Table 1**. All NFAs exhibit broad absorption range from 600 to 900 nm in both the solution and solid state. In detail, compared to **INPIC-4F** with absorption maximum at 821 nm, ***m*-INPOIC** shows a slightly blue-shifted absorption with absorption maximum at 805 nm, while ***p*-INPOIC** peaks at 823 nm. Furthermore, the absorption peak of ***m*-INPOIC**, ***p*-INPOIC** and **INPIC-4F** films red-shifted by ~37 nm, 44 nm and 52 nm in comparison with that in their chloroform solutions, respectively, implying that ***m*-INPOIC** exhibited a more dispersed molecular aggregation than the other two isomers, which is constant with the results from DFT simulation. Moreover, the optical bandgap (E_g^{opt}) of ***m*-INPOIC** and ***p*-INPOIC** was estimated to be 1.41 and 1.37 eV, respectively, close to that of **INPIC-4F** (E_g^{opt} = 1.39 eV). The electrochemical cyclic voltammetry (CV) measurements were conducted to evaluate the electrochemical properties of NFAs, with the CV curves shown in **Fig. S7d** (ESI†). The highest occupied molecular orbital (HOMO) and lowest unoccupied molecular orbital (LUMO) energy levels were thus calculated from redox peak potentials. The HOMO/LUMO levels of ***m*-INPOIC** and ***p*-INPOIC** are calculated to be -5.41 eV/-3.97 eV and -5.38 eV/-4.00 eV, respectively (**Table 1**). These two alkoxy-substituted NFAs have slightly down-shifted LUMO levels but up-shifted HOMO levels in comparison to **INPIC-4F**, as clearly observed from the energy level diagrams **Fig. 2b**. The electrochemical bandgap (E_g^{CV}) values agree well with those E_g^{opt} ones for all NFAs.

To verify the aforementioned discussion, grazing-incidence wide-angle X-ray scattering (GIWAXS) measurement was performed to investigate the molecular ordering and texture of neat NFAs in solid state. As depicted in **Fig. 1b&1c**, the neat **INPIC-4F** show strong lamellar (100) and (200) and π-π stacking peaks in out-of-plane orientation, indicative of anisotropic packing in face-on and edge-on orientation, which is constant with the literature reported by Wang et al.[31] After introducing oxygen atoms into alkylphenyl sidechain, this phenomenon is slightly decreased (weaker lamellar peak intensity in OOP direction). In contrast, after change the alkoxyl sidechain position from *para* to *meta*, the textures of the ***m*-INPOIC** is remarkably different from that of ***p*-INPOIC**. Specifically, a well-defined (010) reflection peak at q~ 1.78 Å^{-1} only appears in OOP direction of ***m*-INPOIC**, accompanied by the appearance of (100) peak in in-plane direction, suggesting a highly face-on crystal packing with respect to the substrate, which is similar to the previously reported high-efficiency NFA system.

Table 1 Optical, electrochemical and thermal properties of three acceptors

Acceptors	λ_{max} [nm][a]	λ_{max} [nm][b]	λ_{onset} [nm][b]	E_g^{opt} [eV][c]	HOMO [eV]	LUMO [eV]	E_g^{CV} [eV]	T_d [°C]
INPIC-4F	769	821	892	1.39	-5.42	-3.94	1.48	332
***p*-INPOIC**	779	823	905	1.37	-5.38	-4.00	1.38	377
***m*-INPOIC**	773	810	879	1.41	-5.41	-3.97	1.44	376

[a]In chloroform solution (conc. 10^{-5} M); [b]in thin film; [c]E_g^{opt} =1240/λ_{onset}.

As the conjugation properties is one of the vital part of evaluating organic semiconductors. In particular, the information of π-π stacking ($d_{π-π}$) and coherence length (L_c) in OOP direction is extremely important for organic photovoltaic material. The IP and OOP profiles from GIWAXS patterns are shown in **Fig. 1c**. We evaluated that the smallest $d_{π-π}$ was obtained from ***m*-INPOIC** neat films ($d_{π-π}$ = 3.53 Å) in comparison with that of INPIC-4F ($d_{π-π}$ = 4.00 Å) and ***p*-INPOIC** ($d_{π-π}$ = 3.88 Å). However, from the absorption spectra, the redshift of ***m*-INPOIC** from solution to thin-film is the smallest relative to other two counterparts, suggesting the weakest π-π stacking in ***m*-INPOIC**. These two results can not be self-constant, thus, we speculated that the information in the OOP

direction does not fully represent the information of the **INPIC-4F** and ***p*-INPOIC** since these two materials present the mixed crystalline property and anisotropic packing. Furthermore, the coherence length features a positive relationship with the conjugation and planarity of materials. As calculated from OOP profiles, the Lc values of three materials are 5.2 nm, 3.4 nm and 2.4 nm, respectively. Therefore, ***m*-INPOIC** exhibits the minimum degree of conjugation in comparison with that of **INPIC-4F** and ***p*-INPOIC**, which is in accordance with the DFT results about the most flexible geometry in ***m*-INPOIC** molecules. However, we hypothesized that the suppressed crystallinity of ***m*-INPOIC** is advantageous for "molecular organization" to form the optimal hierarchical morphology, which is beneficial for the charge transport and extraction.[34,35]

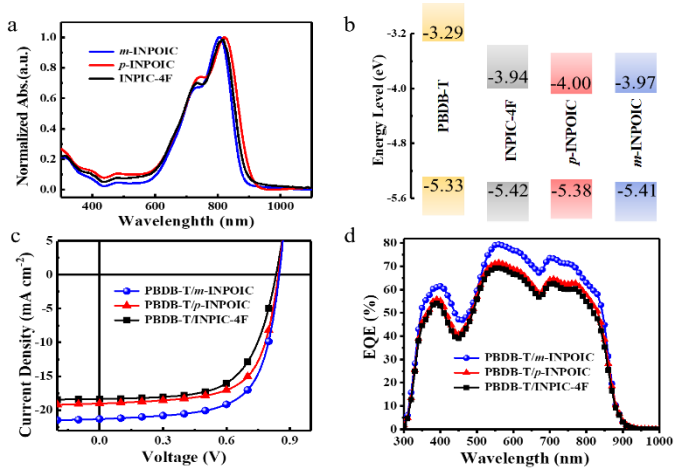

Fig. 2 (a) UV-vis absorption spectra of three NFAs in thin films; (b) Energy levels diagram of PBDB-T and three NFAs. (c) *J*-*V* curves of the best-performing PBDB-T/NFA OSCs under AM 1.5 G illumination. (d) EQE plots of the corresponding optimized devices.

To investigate the photovoltaic performance of these novel acceptors, bulk-heterojunction (BHJ) OSCs were fabricated with an inverted structure of indium tin oxide (ITO)/ZnO/active layer/MoO_x/Ag. The polymer PBDB-T was selected as electron donor due to its complementary absorption and well matched energy levels with our acceptors. Chlorobenzene (CB) was selected as processing solvent. Notably, after dissolving the donor and acceptor in CB solvent in 80 °C, then all devices were constructed without addition of any processing additives and annealing treatment. The effect of D/A weight ratio (1:0.8~1:1.2) and active layer thickness (85~252 nm) on device performance was studied, and the detailed optimization processes are summarized in the Supporting Information (**Table S1** and **Table S2**, ESI†). Upon systematic device optimizations, the promising D/A blend ratio for binary devices was found to be 1:1 (weight ratio), and optimal thickness of active layer is ≈102 nm.

The *J*-*V* characteristics of the optimized devices based on three NFAs are plotted in **Fig. 2c**, with the corresponding photovoltaic parameters listed in **Table 2**. The PBDB-T:***m*-INPOIC** as-cast devices exhibited a promising PCE of 12.1%, with a short-circuit current density (J_{sc}) of 21.3 mA cm^{-2}, open-circuit voltage (V_{oc}) of 850 mV, and fill factor (FF) of 66.9%, respectively. In contrast, PBDB-T:***p*-INPOIC** and PBDB-T:**INPIC-4F** as-cast devices yielded a moderate PCE of 10.6% and 9.71%, respectively. As illustrated in Table S1, the ***m*-INPOIC** devices exhibit significantly improved J_{sc} than ***p*-INPOIC** and PBDB-T:**INPIC-4F** counterparts. Meanwhile, alkoxylated ***m*-INPOIC** and ***p*-INPOIC** based OSCs present 15 and 11 mV increased V_{oc} in comparison to that of alkylated INPIC-4F device. The tolerance of device performance to active layer thickness was further investigated with the optimized D/A (1:1) ratio, where the thickness (85 ~ 252 nm) was controlled by the solution concentrations and spin-coating speed. The variation of PCEs for three NFAs as-cast OSCs with active layer thickness can be found in **Fig. 5d**. Generally, the thicker the active layer, the more severe recombination will appear, resulting in a decreased FF and PCE for devices.[20] However, PBDB-T/***m*-INPOIC** (1:1, w/w) based devices exhibit over 11% PCE with 85~206 nm active layers and 10.2% still obtained even with 250 nm thicker blend film, while ***p*-INPOIC** and **INPIC-4F** based devices decreased from 10.6% to 6.58% and from 9.71% to 5.57%, respectively. The good tolerance of PBDB-T/***m*-INPOIC** based OSCs to film thickness should be ascribed to the balanced charge transport and the lower bimolecular recombination in blend films.[36]

Table 2 Device parameters of the optimized PBDB-T/NFA (1:1, w/w) OSCs

Active layer (102 nm)	J_{sc} [mA cm^{-2}]	J_{sc} [a)] [mA cm^{-2}]	V_{OC} [mV]	FF [%]	PCE [%]	PCE [b)] [%]
PBDB-T:***m*-INPOIC**	21.3	20.7	850	66.9	12.1	11.8
PBDB-T:***p*-INPOIC**	19.0	18.4	846	66.1	10.6	10.4
PBDB-T:**INPIC-4F**	18.4	17.9	835	63.2	9.71	9.64

[a)] J_{sc} integrated from EQE curves in Figure 2b; [b)] average PCEs from 10 devices.

The external quantum efficiency (EQE) curves of the corresponding optimized devices are shown in **Fig. 2d**. Obviously, all the EQE plots exhibit a broad photoresponse range from 300 to 900 nm. The ***m*-INPOIC** based devices exhibit a stronger photon response with higher EQE values in the whole absorption spectrum in comparison to ***p*-INPOIC** and **INPIC-4F** based ones. Especially, PBDB-T/***m*-INPOIC** devices recorded over 70% EQE in the regions of 520-650 nm and 690-760 nm. With the increase of the light-to-current conversion, a greatly improved J_{sc} was thus obtained in ***m*-INPOIC** based devices compared to those of two counterparts.[37] The J_{sc} integrated from EQE curves was determined to be 20.7, 18.4 and 17.9 mA cm^{-2}, respectively, for ***m*-INPOIC**, ***p*-INPOIC** and **INPIC-4F** based devices, which agrees well with the values obtained from the *J*-*V* curves within 5% error.

Fig. 3a presents the photocurrent density (J_{ph}) as a function of effective voltage (V_{eff}) of the OSC devices. In detail, J_{ph} is calculated by the difference between the light current and dark current, J_{sat} represents the saturation current. V_{eff} is given by $V_{eff} = V_0 - V$, where V_0 is the compensation voltage defined as J_{ph} (V_0) = 0, and V is the applied voltage.[38] Compared to **INPIC-4F**, ***m*-INPOIC** and ***p*-INPOIC** based devices possess better charge collection property, due to higher J_{ph} values even at low V_{eff}. The J_{ph}/J_{sat} ratios were calculated to evaluate the exciton dissociation processes in these devices. The J_{ph}/J_{sat} value of ***m*-INPOIC** based

devices was found to be 86%, while 83% and 80% for ***p*-INPOIC** and **INPIC-4F** based devices, respectively. A higher J_{ph}/J_{sat} value in ***m*-INPOIC** based device indicated that the corresponding OSCs feature more efficient exciton dissociation and charge collection processes, leading to higher J_{sc} and FF.[39] The charge recombination processes were investigated by measuring J_{SC} and V_{OC} as a function of light intensity (P_{light}). In general, the relationship of P_{light} and J_{SC} can be defined as $J_{SC} \propto P^S$, and the bimolecular recombination in the devices are negligible when S value is close to 1.[40] In **Fig. 3b**, the S values for the three devices are all 0.99, indicating that the bimolecular recombination is more efficiently suppressed in all three systems. Fitting the relationship of V_{oc} and light intensity, as shown in **Fig. 3c**, the slopes for V_{oc} as a function of light intensity in PBDB-T/***m*-INPOIC** and PBDB-T/***p*-INPOIC** devices are 1.19 and 1.23 kT/q respectively, while that in **INPIC-4F** based devices is calculated to 1.35 kT/q. In general, when the slope is equal to 2 kBT/q, trap-assisted recombination will dominate. In other words, the slope should be equal to 1 kBT/q when the trap-assisted recombination is not a hampered factor in the device. [41] It is clear that the devices based on ***m*-INPOIC** have the lowest trap-assisted recombination, thus an efficient charge extraction can be obtained. From the transient photocurrent curves (**Fig. 3d**), the carrier extraction time for ***m*-INPOIC**, ***p*-INPOIC** and **INPIC-4F** based OSCs is calculated as 0.65, 0.78 and 1.6 μs, respectively. The shorter extraction time in ***m*-INPOIC** based OSCs reveals more efficient charge extraction process occurs in the BHJ blends of PBDB-T:***m*-INPOIC**, which can explain the higher J_{sc} and FF in the corresponding devices.

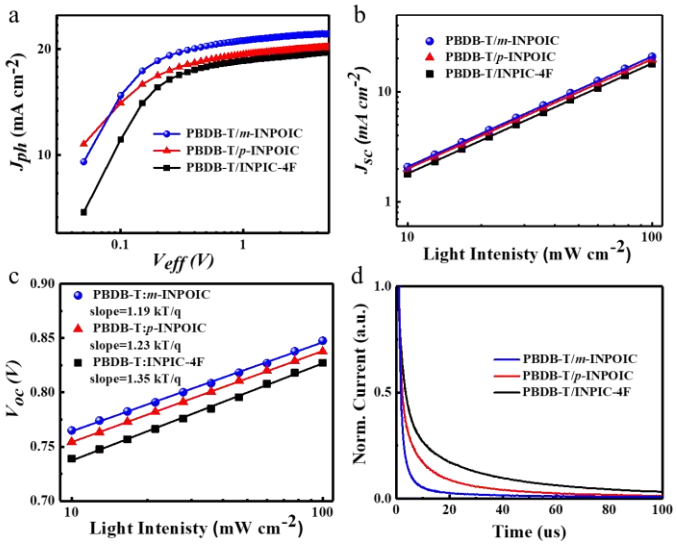

Fig. 3 (a) J_{ph} versus V_{eff}, (b) J_{SC} versus light intensity, (c) V_{OC} versus light intensity, and (d) transient photocurrent curves of designed PBDB-T:NFA OSCs.

To better evaluate the charge transport properties of three BHJ blends, the hole mobility (μ_h) and electron mobility (μ_e) were measured by SCLC method. The mobilities were calculated by fitting the *J*-*V*s from the corresponding hole-only and electron-only devices in the dark condition. As showed in **Fig. S8** and **Table S3** (ESI†), similar μ_h ($2.03\text{-}2.13\times10^{-4}$ cm^2 V^{-1}s^{-1}) was obtained for these blends. On the other hand, the PBDB-T/***m*-INPOIC** blends presented higher electron mobility and more balanced charge mobilities (μ_e = 2.13×10^{-4} cm^2 V^{-1}s^{-1}, μ_h/μ_e = 1.00) than that of PBDB-T/***p*-INPOIC** film (μ_e = 2.06×10^{-4} cm^2 V^{-1}s^{-1}, μ_h/μ_e = 1.00) and PBDB-T:**INPIC-4F** film (μ_e = 8.96×10^{-5} cm^2 V^{-1} s^{-1}, μ_h/μ_e = 2.27). Critically, the improved μ_e and more balanced charge carrier mobility are favorable for more effective charge transport and extraction, thus leading to higher J_{sc} and FF for PBDB-T/***m*-INPOIC** based OSCs.[42]

Since the device performance is strongly correlated to the morphology of blend film, we conducted a series of investigation of morphological characterization to correlate the morphology-performance relationship. Atomic force microscopy (AFM) was firstly utilized to detect the surface morphology of the three blend films. From the AFM images (**Fig. 4a**), the root-meant-square roughness (RMS) values of three blend films based on ***m*-INPOIC**, ***p*-INPOIC** and **INPIC-4F** are 1.86, 3.21, 4.78 nm, respectively. The suitable rough surface formed in ***m*-INPOIC** blend film was caused by the enhanced solubility and favorable crystallinity, which could explain the higher FF in the corresponding devices.[43] Seen from TEM images (**Fig. 4b**), ***m*-INPOIC** blend film maintained appropriate domain sizes and presented an optimal phase separation, while big domains can be observed in **INPIC-4F** and ***p*-INPOIC** blends. The appropriate nanoscale phase separation properties would benefit for exciton separation, thus leading to higher J_{sc} and FF.

The molecular packing in blend films was also characterized by GIWAXS. As seen from **Fig. S9** (ESI†), the π-π stacking diffraction peak of PBDB-T in the OOP direction is more pronounced than those in the IP direction, indicating a preferential face-on orientation. In blend state, as shown in **Fig. 4c** and **4d**, the crystalline feature constitutes of diffraction signals from both PBDB-T and three NFAs. Especially, PBDB-T:***m*-INPOIC** presents higher lamellar (100) and π-π stacking (010) peak intensities relative to the other two films, revealing that higher molecular ordering is formed in the PBDB-T:***m*-INPOIC** blend. The π-π stacking distance ($d_{\pi\text{-}\pi}$) was evaluated to quantize the crystallinity of three blend films. We found that ***m*-INPOIC** blend film has the smallest $d_{\pi-\pi}$ of 3.61 Å, indicating that ***m*-INPOIC** exhibits the strongest intermolecular π-π stacking. Moreover, a sharp diffraction located at q_z = 0.4-0.5 Å^{-1} in the OOP direction was observed in ***p*-INPOIC** or **INPIC-4F** blends, which is assigned to edge-on lamellar stacking of the corresponding acceptor. This implies that ***p*-INPOIC** and **INPIC-4F** blends have both edge-on and face-on packing modes, while PBDB-T:***m*-INPOIC** blend shows predominant face-on orientation. The uniform molecular order would promote the intimate contact between donors and acceptors for efficient charge extraction, thus leading to higher J_{sc} and FF.[28]

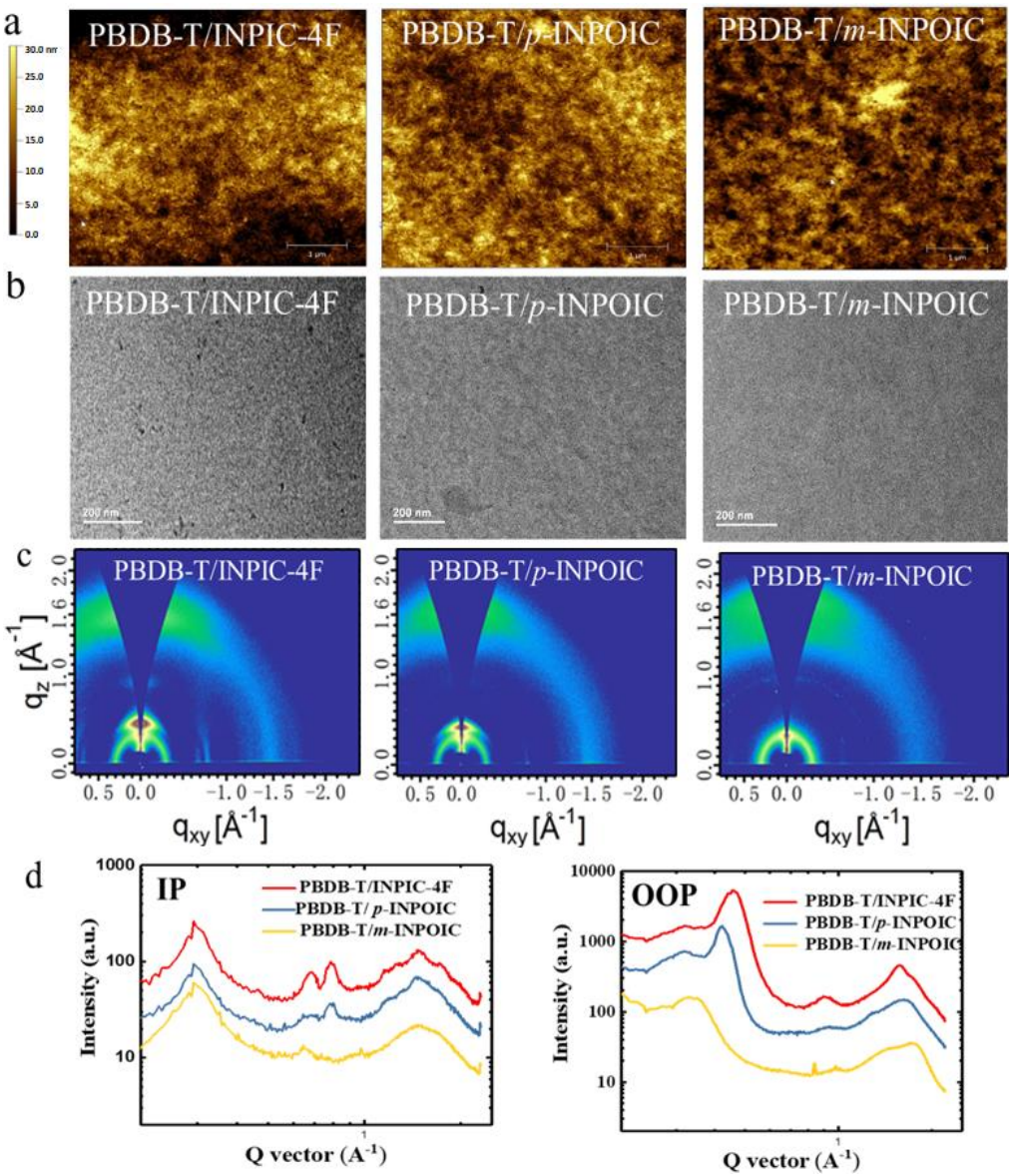

Fig. 4 (a) AFM images of three blend films. (b) TEM images of three blend films. (c) 2D GIWAXS patterns of three blend films. (d) 1D GIWAXS line-cuts of the blends in IP and OOP direction.

According to previous research, ternary strategy has shown great potential to further improve the photovoltaic performance of OSC devices.[44] Our recent study shows that a carefully selected third component is beneficial for both charge generation and transport to achieve a concomitant improvement in all photovoltaic parameters in ternary devices.[45] $PC_{71}BM$ is reported to work as transport channel while NFA forms the intricate phase-separated pathway network in ternary OSCs, leading to better carrier generation and transport.[46] Considering the PCE of as-cast PBDB-T:***m*-INPOIC** based OSCs was limited by the moderate FF (66.9%), further device optimization was explored by incorporating the third component $PC_{71}BM$ as a solid processing-aid into the binary system. The influence of $PC_{71}BM$ incorporation into PBDB-T/***m*-INPOIC** blends was carefully optimized. **Fig. 5a** and **5b** depict the *J*-*V* characteristics and EQE curves for the resulting ternary devices with the addition of 15 wt% and 30 wt% $PC_{71}BM$. Notably, after incorporating $PC_{71}BM$ into PBDB-T/***m*-INPOIC** blend, a maximum PCE of 14.0% can be obtained for PBDB-T/***m*-INPOIC**/$PC_{71}BM$ (1:1:0.15, w/w/w) ternary device with 162 nm thick active layer, which is the highest value for single-junction as-cast OSCs reported to date (**Fig. 5c**). This statement is made on the basis of our careful survey of the most recent high-efficiency as-cast OSCs (**Table S4, ESI**†). The high performance could be ascribed to the morphology optimization by adding $PC_{71}BM$.[46] Moreover, the EQE results demonstrate that the ternary device possesses higher photon-to-carrier conversion efficiencies than binary systems, which is consistent with higher J_{sc} in ternary devices. A close look at the device parameters of optimized binary and ternary OSCs in **Table 3**, one can find that 15 wt% $PC_{71}BM$ can improve both charge generation and transport in PBDB-T ***m*-INPOIC**, resulting in a concomitant improvement in all photovoltaic parameters in ternary devices.

Table 3 Device photovoltaic parameters of PBDB-T/***m*-INPOIC**/P_{71}BM based OSCs

PBDB-T/***m*-INPOIC**/P_{71}BM (by weight ratio)	J_{sc} [mA cm^{-2}]	J_{sc} [a)] [mA cm^{-2}]	V_{oc} [mV]	FF [%]	PCE [%]	PCE [b)] [%]
1:1:0	21.3	20.7	850	66.9	12.1	11.8
1:1:0.15	22.8	22.1	857	71.6	14.0	13.6
1:1:0.30	20.2	19.6	858	67.3	11.6	11.5

[a)] J_{sc} integrated from EQE curves in Figure 5b; [b)] average PCEs from 10 devices.

To further evaluate the potential of practical application, the optimal PBDB-T/***m*-INPOIC**/$PC_{71}BM$ (1:1:0.15, w/w/w) ternary OSCs was explored in a wide range of active layer thickness from 82 to 342 nm. The detailed device parameters are listed in **Table S2**. As shown in **Fig. 5c** & **5d**, all photovoltaic parameters are insensitive to the increase of active layer thickness in the region of 82-202 nm, where high J_{sc} (~22 mA cm^{-2}) and FF (~70%) values were achieved to afford PCEs over 13% even with 202 nm thick active layers. These results are even better than all reported best-performing as-cast OSCs with active layers thinner than 110 nm (**Fig. 5c**). Notably, ***m*-INPOIC** based ternary devices deliver over 11% PCEs even with active layers thicker than 300 nm, indicating its good tolerance to film thickness. The correlation of device performance with thickness of active layers for all as-cast devices of three NFAs OSCs is presented in **Fig. 5d** for direct comparison. The optimal thickness of active layer was found to be 102 nm for all three NFAs based binary OSCs while 162 nm for ternary devices. Both binary and ternary devices based on ***m*-INPOIC** exhibit higher PCEs than ***p*-INPOIC** and **INPIC-4F** based devices at the same thickness of active layer. PCEs over 11% can be readily achieved in wide windows of blend film thickness, i.e., no thicker than 206 nm or 302 nm for ***m*-INPOIC** as-cast binary or ternary OSCs, respectively. The excellent tolerance of ***m*-INPOIC** as-cast OSCs to active layer thickness makes it attractive for mass production of large area devices with industrial solution-processing techniques.

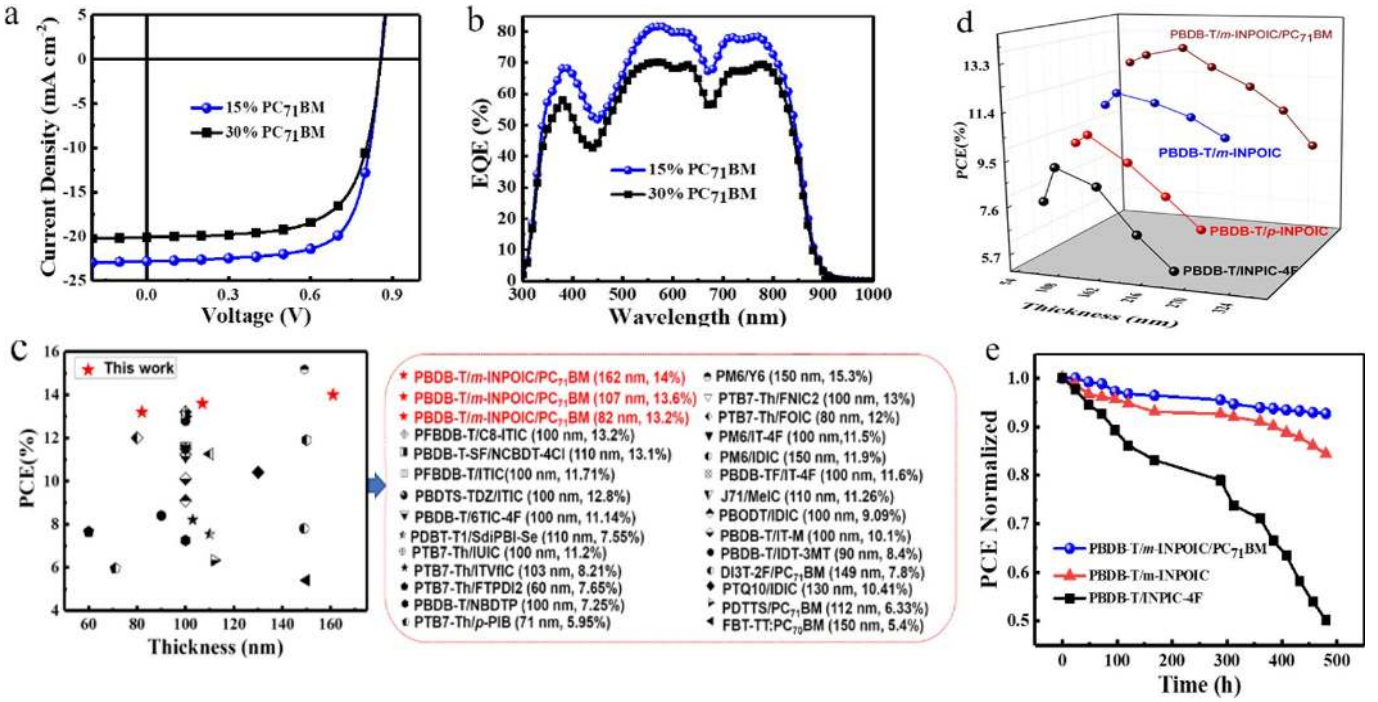

Fig. 5 (a) *J-V* curves and (b) EQE plots of the corresponding optimized ternary devices. (c) PCE as a function of thickness for our as-cast device and as-cast OSCs reported in literature. Source references for the data points are provided in Table S4 in ESI. (d) PCEs as a function of active layer thickness for our NFAs based devices. (e) Stability test for binary and ternary devices

The device stability of the optimal ternary OSCs was also investigated and compared with the best-performing binary devices based on ***m*-INPOIC** and **INPIC-4F**. As shown in **Fig. 5e**, all ***m*-INPOIC** based devices exhibited much better stability than **INPIC-4F** based ones within the continuous monitoring of device performance in nitrogen atmosphere for 480 hours. A PCE retention over 95% and 84% was observed for ***m*-INPOIC** binary and ternary OSCs, while only 50% was found for **INPIC-4F** devices. The stability of ***m*-INPOIC** devices may be attributed to unified molecular orientation of ***m*-INPOIC**, as revealed by GIWAXS (**Fig. 1b**&**1c**). The incorporation of $PC_{71}BM$ endows PBDB-T/***m*-INPOIC** with even better device stability, indicated by the level-off PCEs of ternary devices after a slow decrease in the first 100-hour-storage. For such ternary blends of donor/NFA/$PC_{71}BM$, the $PC_{71}BM$ phase is revealed to separate with the donor and NFA to form morphological framework and provide efficient electron mobility, and the donor and NFA form a smaller size phase separation that fits into the $PC_{71}BM$ mesh network.[46] In this case, the incorporated $PC_{71}BM$ works as carrier transporting highway and protector to stabilize the donor/NFA phase-separated interpenetrating network. As a result, higher J_{SC} and FF values can be achieved in ternary devices in comparison to the corresponding donor/NFA

binary ones (**Table 3**). More importantly, the ternary OSCs can also harvest significantly enhanced device stability (**Fig. 5e**). The dual advantage of carefully added $PC_{71}BM$ to improve both OSCs performance and stability suggests the great potential for our molecular orientation unified ***m*-INPOIC** to be explored in solution-processing large area of high-efficiency yet stable as-cast OSCs in wide windows of active layer thickness.

3. Conclusion

We have designed a *meta*-alkoxyphenyl substituted nonfullerene acceptor (***m*-INPOIC**) to unify face-on molecular orientation, which realized over 13% efficiencies for as-cast single-junction solar cells in a wide range of active layer thickness (82~202 nm). The impact of introduction and positioning of alkoxy sidechains was systematically investigated in comparison with the *para*-alkoxy substituted ***p*-INPOIC** and *para*-alkylphenyl substituted **INPIC-4F**. The ***m*-INPOIC** presents predominant face-on orientation in films and higher electron mobility than two counterparts. The as-cast PBDB-T/***m*-INPOIC** binary OSCs show a PCE of 12.1 %, with a short-circuit current density (J_{sc}) of 21.3 mA cm^{-2}, open-circuit voltage (V_{oc}) of 850 mV, and fill factor (FF) of 66.9 %. The as-cast devices were further optimized by incorporating $PC_{71}BM$ as solid processing-aid to improve charge transport and morphology stability in ternary blends, a maximum PCE of 14.0% was obtained with a good tolerance to film thickness and enhanced device stability. The design strategy manifests the benefits of unifying molecular orientation of NFA and incorporating $PC_{71}BM$ in blend films for high-efficiency as-cast OSCs.

Conflicts of interest

There are no conflicts to declare.

Acknowledgements

The authors would like to thank the financial support from the National Natural Science Foundation of China (Grant No. 51573077, 21875111 and 51861145401), Jiangsu Province Natural Science Foundation (BK20180496), the 333 Project to Cultivate High Level Talents in Jiangsu Province, and the Priority Academic Program Development of Jiangsu Higher Education Institutions.

References

1 Y.-J. Cheng, S.-H. Yang, C.-S. Hsu, *Chem. Rev*., 2009, **109**, 5868-5923.
2 G. Li, R. Zhu and Y. Yang, *Nat. Photon.*, 2012, **6**, 153-161.
3 L. Lu, T. Zheng, Q. Wu, A. M. Schneider, D. Zhao and L. Yu, *Chem. Rev*., 2015, **115**, 12666-12731.
G. Zhang, J. Zhao, P.C.Y. Chow, K. Jiang, J. Zhang, Z. Zhu, J. Zhang, F. Huang and H. Yan, *Chem. Rev.*, 2018, **118**, 3447-3507.
2. J. Hou, O. Inganas, R. H. Friend and F. Gao, *Nat. Mater.*, 2018, **17**, 119-128.
3. H. Sun, F. Chen, Z. Chen, *Mater. Today*, 2018, DOI :10.1016/j.mattod.2018.09.004
4. R. Yu, H. Yao and J. Hou, *Adv. Energy Mater.*, 2018, **8**, 1702814.
5. C. Yan, S. Barlow, Z. Wang, H. Yan, A.K.Y. Jen, S.R. Marder and X. Zhan, *Nat. Rev. Mater.*, 2018, **3**, 18003.
6. J. Yuan, Y. Zhang, L. Zhou, G. Zhang, H.L. Yip, T. Lau, X. Lu, C. Zhu, H. Peng, P. Johnson, M. Leclerc, Y. Cao, J. Ulanski, Y. Li and Y. Zou, *Joule*, 2019, DOI: 10.1016/j.joule.2019.01.004.
7. L. Meng, Y. Zhang, X. Wan, C. Li, X. Zhang, Y. Wang, X. Ke, Z. Xiao, L. Ding, R. Xia, H.L. Yip, Y. Cao and Y. Chen, *Science*, 2018, **361**, 1094-1098.
8. H. Zhang, H. Yao, J. Hou, J. Zhu, J. Zhang, W. Li, R. Yu, B. Gao, S. Zhang and J. Hou, *Adv. Mater.*, 2018, **30**, 1800613.
9. S. Zhang, Y. Qin, J. Zhu and J. Hou, *Adv. Mater.*, 2018, **30**, 1800868.
10. Y. Zhang, B. Kan, Y. Sun, Y. Wang, R. Xia, X. Ke, Y.Q. Yi, C. Li, H.L. Yip, X. Wan, Y. Cao and Y. Chen, *Adv. Mater.*, 2018, **30**, 1707508.
11. C. McDowell, M. Abdelsamie, M.F. Toney and G.C. Bazan, *Adv. Mater.*, 2018, **30**, 1707114.
12. W. Wang, L. Song, D. Magerl, D. Moseguí González, V. Korstgens, M. Philipp, J.-F. Moulin and P. Muller-Buschbaum, *Adv. Funct. Mater.*, 2018, **28**, 1800209.
13. Z. Zheng, O.M. Awartani, B. Gautam, D. Liu, Y. Qin, W. Li, A. Bataller, K. Gundogdu, H. Ade and J. Hou, *Adv. Mater.*, 2017, **29**, 1604241.
14. Q. Zhang, B. Kan, F. Liu, G. Long, X. Wan, X. Chen, Y. Zuo, W. Ni, H. Zhang, M. Li, Z. Hu, F. Huang, Y. Cao, Z. Liang, M. Zhang, T. P. Russell and Y.Chen, *Nat. Photon.*, 2014, **9**, 35-41.
15. S. Mukherjee, C.M. Proctor, G.C. Bazan, T.-Q. Nguyen and H. Ade, *Adv. Energy Mater.*, 2015, **5**, 1500877.
16. W. Wang, B. Zhao, Z. Cong, Y. Xie, H. Wu, Q. Liang, S. Liu, F. Liu, C. Gao, H. Wu and Y. Cao, *ACS Energy Lett.*, 2018, **3**, 1499-1507.
17. V. Turkovic, S. Engmann, N. Tsierkezos, H. Hoppe, U. Ritter and G. Gobsch, *ACS Appl. Mater. Interfaces*, 2014, **6**, 18525-18537.
18. B.J. Tremolet de Villers, K.A. O'Hara, D.P. Ostrowski, P.H. Biddle, S.E. Shaheen, M.L. Chabinyc, D.C. Olson and N. Kopidakis, Chem. Mater., 2016, **28**, 876-884.
19. R. Yu, H. Yao, L. Hong, Y. Qin, J. Zhu, Y. Cui, S. Li and J. Hou, *Nat. Commun*., 2018, **9**, 4645.
20. Y. Zang, Q. Xin, J. Zhao and J. Lin, *J. Phys. Chem. C*, 2018, **122**, 16532-16539.
21. G. Zhang, R. Xia, Z. Chen, J. Xiao, X. Zhao, S. Liu, H.L. Yip and Y. Cao, *Adv. Energy Mater.*, 2018, **8**, 1801609.
22. P. Yin, T. Zheng, Y. Wu, G. Liu, Z.-G. Zhang, C. Cui, Y. Li and P. Shen, *J. Mater. Chem. A,* 2018, **6**, 20313-20326
23. Y. Yang, K. Wang, G. Li, X. Ran, X. Song, N. Gasparini, Q.Q. Zhang, X. Lai, X. Guo, F. Meng, M. Du, W. Huang, D. Baran, Small, 2018, **14**, 1801542.
24. E. Voroshazi, I. Cardinaletti, T. Conard and B. P. Rand, *Adv. Energy Mater.*, 2014, **4**, 1400848.
25. J. Wang, J. Zhang, Y. Xiao, T. Xiao, R. Zhu, C. Yan, Y. Fu, G. Lu, X. Lu, S.R. Marder and X. Zhan, *J. Am. Chem. Soc.,* 2018, **140**, 9140-9147.
26. Q. Fan, Y. Wang, M. Zhang, B. Wu, X. Guo, Y. Jiang, W. Li, B. Guo, C. Ye, W. Su, J. Fang, X. Ou, F. Liu, Z. Wei, T. Ch. Sum, T. P. Russell, Y. Li, *Adv. Mater.*, 2018, **30**, 1704546.
27. Z. Zhang, L. Feng, S. Xu, Y. Liu, H. Peng, Z.G. Zhang, Y. Li and Y. Zou, *Adv. Sci.*, 2017, **4**, 1700152.
28. H. Yao, Y. Chen, Y. Qin, R. Yu, Y. Cui, B. Yang, S. Li, K. Zhang and J. Hou, *Adv. Mater.*, 2016, **28**, 8283-8287.

29. Y. Cui, C. Yang, H. Yao, J. Zhu, Y. Wang, G. Jia, F. Gao and J. Hou, *Adv. Mater.*, 2017, **29**, 1703080.
30. J. Sun, X. Ma, Z. Zhang, J. Yu, J. Zhou, X. Yin, L. Yang, R. Geng, R. Zhu, F. Zhang and W. Tang, *Adv. Mater.*, 2018, **30**, 1707150.
31. W. Li, M. Chen, Z. Zhang, J. Cai, H. Zhang, R.S. Gurney, D. Liu, J. Yu, W. Tang and T. Wang, *Adv. Funct. Mater.*, 2018, **28**, 1807662.
32. W. Su, Q. Fan, X. Guo, J. Chen, Y. Wang, X. Wang, P. Dai, C. Ye, X. Bao, W. Ma, M. Zhang and Y. Li, *J. Mater. Chem. A*, 2018, **6**, 7988-7996.
33. Y. Liu, M. Li, X. Zhou, Q.-Q. Jia, S. Feng, P. Jiang, X. Xu, W. Ma, H.-B. Li and Z. Bo, *ACS Energy Lett.*, 2018, **3**, 1832-1839.
34. F. Zhao, C. Wang and X. Zhan, *Adv. Energy Mater.*, 2018, **8**, 1703147.
35. J.R. Tumbleston, B.A. Collins, L. Yang, A.C. Stuart, E. Gann, W. Ma, W. You and H. Ade, *Nat. Photon.*, 2014, **8**, 385-391.
36. B. Fan, P. Zhu, J. Xin, N. Li, L. Ying, W. Zhong, Z. Li, W. Ma, F. Huang and Y. Cao, *Adv. Energy Mater.*, 2018, **8**, 1703085.
37. W. Li, L. Ye, S. Li, H. Yao, H. Ade and J. Hou, *Adv. Mater.*, 2018, **30**, 1707170.
38. N. Gasparini, M. Salvador, S. Strohm, T. Heumueller, I. Levchuk, A. Wadsworth, J.H. Bannock, J.C. de Mello, H.-J. Egelhaaf, D. Baran, I. McCulloch and C.J. Brabec, *Adv. Energy Mater.*, 2017, **7**, 1700770.
39. J. Zhang, F. Liu, S. Chen, C. Yang, X. Zhu and D. Zhu, *Macromol. Rapid. Commun.* 2018, **39**, 1800393.
40. Y. Yang, J. Wang, H. Xu, X. Zhan and X. Chen, *ACS Appl. Mater. Interfaces*, 2018, **10**, 18984-18992.
41. X. Song, N. Gasparini, L. Ye, H. Yao, J. Hou, H. Ade and D. Baran, *ACS Energy Lett.* 2018, **3**, 669-676.
42. D. Liu, B. Yang, B. Jang, B. Xu, S. Zhang, C. He, H.Y. Woo and J. Hou, *Energy Environ. Sci.,* 2017, **10**, 546-551.
43. W. Gao, T. Liu, R. Ming, Z. Luo, K. Wu, L. Zhang, J. Xin, D. Xie, G. Zhang, W. Ma, H. Yan and C. Yang, *Adv. Funct. Mater.* 2018, **28**, 1803128.
44. T. Liu, Z. Luo, Q. Fan, G. Zhang, L. Zhang, W. Gao, X. Guo, W. Ma, M. Zhang, C. Yang, Y. Li and H. Yan, *Energy Environ. Sci.*, 2018, **11**, 3275-3282.
45. X. Song, N. Gasparini, M. Nahid, S. Paleti, J. Wang, H. Ade and D. Baran, *Joule*, accepted in January 2019.
46. Z. Zhou, S. Xu, J. Song, Y. Jin, Q. Yue, Y. Qian, F. Liu, F. Zhang and X. Zhu, *Nat. Energy*, 2018, **3**, 952-959.

Table of Content